Formation and decay of ^{200}Pb* using different incoming channels

Rajni,[1] Raj Kumar,[2] and Manoj K. Sharma[1]
[1]*School of Physics and Materials Science, Thapar University, Patiala-147004, India*
[2]*Department of Physics and Astronomy, University of Padova, I-35131 Padova, Italy*
(Received 17 February 2014; revised manuscript received 12 July 2014; published 7 October 2014)

Entrance channel effect is studied in the dynamics of ^{200}Pb* formed in ^{16}O + ^{184}W, ^{19}F + ^{181}Ta, and ^{30}Si + ^{170}Er reactions over a wide range of excitation energies using the dynamical cluster-decay model (DCM) and Wong model. The effect of deformations up to β_2 along with optimum orientation is investigated in both formalisms. The fusion cross section is studied using the Wong model, which overestimates experimental data for ^{19}F + ^{181}Ta and ^{30}Si + ^{170}Er reactions and underestimates the data at few energies for ^{16}O + ^{184}W. However with the use of the extended ℓ-summed Wong model, the overestimation is taken care and the cross sections are fitted nicely. The Wong-based calculations suggest that there might be some noncompound nucleus contribution at few energies for the ^{16}O + ^{184}W channel, as the underestimation of the cross section persists even after the inclusion of deformation effects. This lead us to conclude that the formation of ^{200}Pb* compound nucleus depends on the choice of the incoming channel. In addition to this, the decay path of ^{200}Pb* is investigated using DCM. Although the overall decay pattern of compound nucleus ^{200}Pb* seems similar for all the chosen reactions, some signatures of variation are observed in fission and in the intermediate mass fragment region for the deformed fragmentation process. It is to be noted that with the inclusion of deformation, the decay pattern changes from symmetric to asymmetric, thereby suggesting that the deformation and orientation of decaying fragment are equally important in the formation as well as in the decay process of proton magic nuclear system ^{200}Pb*. Prediction of the evaporation residue and fission cross sections at higher as well as at lower incident energies is also worked out. In addition to this, the dynamics of neighboring nuclei ^{192}Pb* and ^{202}Pb* is also analyzed.

DOI: 10.1103/PhysRevC.90.044604 PACS number(s): 25.70.Jj, 25.60.Pj, 24.10.−i, 27.80.+w

I. INTRODUCTION

Entrance channel effect on fusion-fission dynamics was studied for many years. Yet this concept draws much interest because of many open questions in the related area. Depending on the entrance channel mass asymmetry and deformation involved, the dynamical path to fusion-fission process differs significantly. The complex process of the fusion of two heavy nuclei can be best understood via the decay products of compound nucleus (CN), such as the fusion-evaporation residue (ER), complex-intermediate mass fragment (IMF), and fusion-fission (ff) process. The ff comprises either symmetric fission, asymmetric or near-symmetric fission (nSF) and/or heavy mass fragment (HMF). In addition to the CN process some noncompound nucleus (nCN) processes such as deep inelastic collision (DIC), quasifission (qf), incomplete fusion (ICF), etc., may also occur depending upon the beam energy, mass asymmetry, and nature of projectile used. It is worth noting that qf occurs at the early stage of the collision when two fragments are linked by a neck and nucleon start shifting from the heavy fragment towards the lighter one. The two fragments then get re-separated with the same or higher mass symmetry than the entrance channel, without forming a CN. In fact, the qf process is a dynamical mechanism depending on the characteristics of the entrance channel, while CN fission is purely statistical and is determined by the temperature and angular momentum involved. The fusion-fission process of the incoming channel depends upon the barrier formed by different potentials like long-range Coulomb and short-range nuclear potentials. The incoming projectile must have sufficient energy to cross the barrier, which indicates that the barrier characteristics are important for studying the ff process.

Earlier, experiments [1,2] were performed at different center-of-mass energies ($E_{\rm c.m.}$) ranging from 107.40 MeV to 136.96 MeV to measure the ER and fusion cross section of the spherical compound nucleus ^{200}Pb*, formed in reaction with the ^{30}Si projectile and ^{170}Er target. Because ^{200}Pb* is a spherical and stable system with magic Z, so it is of interest to study the role of deformation in the decay and formation of the ^{200}Pb* nucleus. The same CN was formed using ^{16}O + ^{184}W and ^{19}F + ^{181}Ta [1,3,4] with $E_{\rm c.m.}$ ranging from 77.19 to 110.56 MeV. Because at $\ell = 0\hbar$, the nucleus-nucleus interaction potential for the relatively asymmetric system is wider and deeper, so the measured cross sections of the fissionlike and ER fragment for the ^{16}O + ^{184}W reaction are larger than those for ^{19}F- and ^{30}Si-induced reactions. These facts directly indicate the experimental signature of the entrance channel effect in ^{200}Pb* nucleus, which motivates us further to study the role of the entrance channel in the decay and formation of ^{200}Pb*. For a long time, the Wong formula [5] has been used for calculating the fusion cross section. In the present work, we have used the Wong formula and its extended version [6–9] to study the fusion process of ^{200}Pb*. To study the entrance channel dependence on the decay pattern, we used the dynamical cluster-decay model (DCM) [10–21]. This model employs neck-length parameter (ΔR) for addressing the data, which leads to required modification of the barrier at the near- and subbarrier region.

In the present work, we observe that the Wong formula overestimates or underestimates the data, whereas its extended version, i.e., the ℓ-summed extended Wong model, fits the experimental fusion cross section nicely for the three incident channels except at few energies of the ^{16}O + ^{184}W reaction.

However, fitting is improved slightly with the inclusion of the deformation effect. It is anticipated that there might be some noncompound nucleus (nCN) contribution at two or three energies for the ^{16}O-induced channel.

For the decay part, DCM gives a nice fit to the experimental ER and fission cross section with a spherical as well as deformed choice of fragments for the reactions $^{16}\mathrm{O}+{}^{184}\mathrm{W}$, $^{19}\mathrm{F}+{}^{181}\mathrm{Ta}$, and $^{30}\mathrm{Si}+{}^{170}\mathrm{Er}$. To see the difference in the decay pattern of CN, the fragmentation potential and preformation probability for the spherical and deformed cases of three incoming channels are worked out at comparable incident energy $E_{\mathrm{c.m.}} \simeq 110$ MeV. The deformation effects are included up to β_2 along with the hot optimum orientations [22]. It is observed that with the inclusion of deformations, decay pattern changes from symmetric to asymmetric. Although the overall pattern of the fragmentation is similar for the three channels, some signatures of the entrance channel dependence are observed in the IMF and fission regions. Furthermore, the prediction of ER and fission cross sections at higher energies (for O- and F-induced reactions) and at lower energies (for Si induced) help us to provide a comprehensive understanding regarding the dynamics of ^{200}Pb*.

The purpose of this paper is to see the impact of the entrance channel in reference to the decay and formation of ^{200}Pb*. Furthermore, to analyze the effect of deformation and orientation, the formation and decay of ^{200}Pb* is worked out in the framework of the Wong model and DCM respectively. The methodology used for calculations is discussed in Sec. II. Calculations and results are described in Sec. III and finally the outcome is summarized in Sec. IV.

II. METHODOLOGY

A. Wong model

The fusion cross section, in terms of angular-momentum ℓ partial waves, for two deformed and oriented nuclei (with orientation angles θ_i), lying in the same planes and colliding with center-of-mass (c.m.) energy $E_{\mathrm{c.m.}}$, is

$$\sigma(E_{\mathrm{c.m.}},\theta_i) = \sum_{\ell=0}^{\ell_{\max}} \sigma_\ell = \frac{\pi}{k^2} \sum_{\ell=0}^{\ell_{\max}} (2\ell+1) P_\ell(E_{\mathrm{c.m.}},\theta_i), \quad (1)$$

with $k = \sqrt{\frac{2\mu E_{\mathrm{c.m.}}}{\hbar^2}}$ and μ is the reduced mass, P_ℓ is the transmission coefficient for each ℓ which describes the penetrability of barrier V_T^ℓ(R), given by

$$V_T^\ell(R) = V_C(R,Z_i,\beta_{\lambda i},\theta_i,T) + V_N(R,A_i,\beta_{\lambda i},\theta_i,T) + V_\ell(R,A_i,\beta_{\lambda i},\theta_i,T), \quad (2)$$

using Hill-Wheeler approximation [23], the penetrability P_ℓ, in terms of its barrier height V_B^ℓ and curvature $\hbar\omega_\ell(E_{\mathrm{c.m.}},\theta_i)$, is

$$P_\ell = \left[1 + \exp\left(\frac{2\pi\left(V_B^\ell - E_{\mathrm{c.m.}}\right)}{\hbar\omega_\ell}\right)\right]^{-1}, \quad (3)$$

with $\hbar\omega_\ell$ evaluated at the barrier position $R = R_B^\ell$ corresponding to barrier height V_B^ℓ, given as

$$\hbar\omega_\ell(E_{\mathrm{c.m.}},\theta_i) = \hbar\left[\left|d^2V_T^\ell(R)/dR^2\right|_{R=R_B^\ell}/\mu\right]^{1/2}, \quad (4)$$

and R_B^ℓ obtained from the condition $|dV_T^\ell(R)/dR|_{R=R_B^\ell} = 0$. Noting that the ℓ-summed expression, i.e., Eq. (1) uses the ℓ-dependent potential [Eq. (2)], its ℓ summation is carried out for the $\ell_{\max}$ determined empirically for a best fit to the measured cross section, and the angle θ_i integrated to give the fusion cross section,

$$\sigma(E_{\mathrm{c.m.}}) = \int_{\theta_i}^{\pi/2} \sigma(E_{\mathrm{c.m.}},\theta_i)\sin\theta_1 d\theta_1 \sin\theta_2 d\theta_2. \quad (5)$$

Instead of solving Eq. (1) explicitly, which requires the complete ℓ-dependent potentials $V_T^\ell(R,\ E_{\mathrm{c.m.}},\ \theta_i)$, Wong [5] carried out the ℓ summation approximately under specific conditions: (i) $\hbar\omega_\ell \approx \hbar\omega_0$ and (ii) $V_B^\ell \approx V_B^0 + \frac{\hbar^2\ell(\ell+1)}{2\mu R_B^{02}}$, which means to assume $R_B^\ell \approx R_B^0$ also. In other words V_B^ℓ and $\hbar\omega_\ell$, are obtained for the $\ell = 0$ case, with V_B^0 given by Eq. (2) at $R = R_B^0$. Using these approximations and replacing the ℓ summation in Eq. (1) by an integral, gives the $\ell = 0$ barrier-based Wong formula,

$$\sigma(E_{\mathrm{c.m.}},\theta_i) = \frac{R_B^{02}\hbar\omega_0}{2E_{\mathrm{c.m.}}} \ln\left\{1 + \exp\left[\frac{2\pi}{\hbar\omega_0}\left(E_{\mathrm{c.m.}} - V_B^0\right)\right]\right\}, \quad (6)$$

which on using Eq. (5), would also give $\sigma(E_{\mathrm{c.m.}})$.

B. The dynamical cluster-decay model (DCM)

The DCM employs the collective coordinates of mass (and charge) asymmetry $\eta = (A_1 - A_2)/(A_1 + A_2)$ [and $\eta_Z = (Z_1 - Z_2)/(Z_1 + Z_2)$], relative separation R, the multipole deformations $\beta_{\lambda i}$, and orientations θ_i $(i = 1,2)$ of two nuclei in the same plane. In DCM, the compound nucleus (CN) decay cross section in terms of partial wave analysis is defined as

$$\sigma = \sum_{\ell=0}^{\ell_{\max}} \sigma_\ell = \frac{\pi}{k^2} \sum_{\ell=0}^{\ell_{\max}} (2\ell+1) P_0^\ell P_\ell, \quad k = \sqrt{\frac{2\mu E_{\mathrm{c.m.}}}{\hbar^2}}, \quad (7)$$

where P_0^ℓ is defined as the probability of the formation of fragments at the compound nucleus state and P_ℓ represents barrier penetrability of decaying fragments.

The preformation probability P_0^ℓ refers to η motion and the penetrability P_ℓ to R motion and $\ell_{\max}$ is the maximum angular momentum, fixed here for the light particle cross section approaching zero, i.e., $\sigma_{\mathrm{ER}}(\ell) \to 0$ at $\ell = \ell_{\max}$. It is to be noted that Eq. (7) is the same as Eq. (1), provided the preformation probability $P_0^\ell = 1$. The other difference between Eqs. (1) and (7) is that penetrability P_ℓ is calculated by using the Hill wheeler approximation [23] in the Wong model, whereas the same in DCM is estimated via the WKB method as discussed later in Eq. (10).

P_0^ℓ for each ℓ is obtained by solving the stationary Schrödinger equation in η, at a fixed R,

$$\left[-\frac{\hbar^2}{2\sqrt{B_{\eta\eta}}}\frac{\partial}{\partial\eta}\frac{1}{\sqrt{B_{\eta\eta}}}\frac{\partial}{\partial\eta} + V(\eta,T)\right]\psi^\nu(\eta) = E_\eta^\nu\psi^\nu(\eta), \quad (8)$$

where $\nu = 0,1,2\ldots$ corresponds to ground state ($\nu = 0$) and excited state solutions. On solving Eq. (8) numerically,

$|\psi^{\nu}(\eta)|^2$ gives the probability P_0^{ℓ} of finding the mass distribution as $P_0^{\ell} \propto |\psi^{\nu}(\eta)|^2$ which for the Boltzmann-like function reads

$$|\psi(\eta)|^2 = \sum_{\nu=0}^{\infty} |\psi^{\nu}(\eta)|^2 \exp\left(\frac{-E^{\nu}}{T}\right). \quad (9)$$

It is evident from above expressions that the temperature effects are duly incorporated in the preformation factor P_0^{ℓ} which is calculated using the collective clusterization method. On the other hand barrier penetrability P_{ℓ} is calculated independently for each decaying fragment. Subsequently the total fusion cross section ($\sigma_{\rm fusion} = \sigma_{\rm ER} + \sigma_{ff}$) is governed via P_0^{ℓ} and P_{ℓ} as shown in Eq. (7). It is relevant to mention here that $\sigma_{\rm ER}$ and σ_{ff} are calculated simultaneously on equal footing using DCM, a nonstatistical description based on quantum mechanical fragmentation theory (QMFT). The DCM has a distinct advantage over available statistical phenomena as much needed nuclear structure information can be extracted in this formalism via the preformation factor.

The penetrability P_{ℓ} is estimated using the WKB integral,

$$P_{\ell} = \exp\left[-\frac{2}{\hbar}\int_{R_a}^{R_b} \{2\mu[V(R) - Q_{\rm eff}]\}^{1/2} dR\right], \quad (10)$$

with $V(R_a,T) = V(R_b,T) = {\rm TKE}(T) = Q_{\rm eff}$ for the entry and exit points of the potential barrier. $Q_{\rm eff}$ is the effective Q value of the decay process and the entry point $R_a = R_1(\alpha_1,T) + R_2(\alpha_2,T) + \Delta R(\eta,T) = R_t(\alpha_i,T) + \Delta R(\eta,T)$, with the radius vectors,

$$R_i(\alpha_i,T) = R_{0i}(T)\left[1 + \sum_{\lambda} \beta_{\lambda i} Y_{\lambda}^{(0)}(\alpha_i)\right], \quad (11)$$

with the temperature dependence of R_{0i}, as in Ref. [24],

$$R_{0i}(T) = \left[1.28A_i^{1/3} - 0.76 + 0.8A_i^{-1/3}\right](1 + 0.0007T^2), \quad (12)$$

where T is related to the incoming center-of-mass energy $E_{\rm c.m.}$ or the compound nucleus excitation energy $E^*_{\rm CN}$ via the entrance channel Q_{in} value, as

$$E^*_{\rm CN} = E_{\rm c.m.} + Q_{in} = aT^2 - T \quad (T \text{ in MeV}). \quad (13)$$

We have used $a = {\rm A}/9$ in this work. $Q_{in} = B_1 + B_2 - B_{\rm CN}$, with binding energies B's taken from [25].

The compound nucleus excitation energy $E^*_{\rm CN}$ gets distributed into total excitation energy TXE and total kinetic energy TKE of the two outgoing fragments at each T as $E^*_{\rm CN} + Q_{\rm out}(T) =$ TKE(T)+TXE(T), then the exit channel fragments can be obtained in the ground state with TKE($T = 0$) [$= Q_{\rm out}(T = 0)$] by allowing the emission of light particle and/or γ rays with an energy, $E_x = Q_{\rm eff}(T) - Q_{\rm out}(T = 0) = {\rm TKE}(T) - {\rm TKE}(T = 0)$ such that, of the remaining excitation energy of the decaying system $[E^*_{\rm CN} + Q_{\rm out}(T)] - E_x = {\rm TKE}(T = 0) + {\rm TXE}(T)$, the TXE($T$) is used in secondary particle emission of light particles from the primary fragments, but is not treated here; instead we compare our calculations with primary, presecondary-evaporation fragment emission data. Thus, by defining $Q_{\rm eff}(T) = B(T) - [B_L(T = 0) + B_H(T = 0)] = {\rm TKE}(T) = V(R_a,T)$, in this model we treat the LP emission at par with the IMF emission. In other words, a nonstatistical dynamical treatment is attempted here for the emission of not only IMFs but also the multiple LPs.

The average TKE(T) can be defined as $\langle {\rm TKE}\rangle = \sum_{\ell=0}^{\ell_{\rm max}} \frac{\sigma_{\ell}(A_2)}{\sigma(A_2)} {\rm TKE}(\ell, A_2)$. For every fragment, the TKE for each ℓ is averaged over its corresponding production cross section σ_{ℓ} with respect to total cross section $\sigma(A_2) = \sum_{\ell=0}^{\ell_{\rm max}} \sigma_{\ell}(A_2)$.

The deformation and orientation dependent fragmentation potential used in Eq. (8), at any temperature T, is given as

$$V(\eta,T) = \sum_{i=1}^{2} V_{\rm LDM}(A_i,Z_i,T) + \sum_{i=1}^{2} \delta U \exp\left(-\frac{T^2}{T_0^2}\right) + V_C(R,Z_i,\beta_{\lambda i},\theta_i,T) + V_N(R,A_i,\beta_{\lambda i},\theta_i,T) + V_{\ell}(R,A_i,\beta_{\lambda i},\theta_i,T). \quad (14)$$

Here, $V_{\rm LDM}$ is the T-dependent liquid drop model energy of Davidson *et al.* [26] and δU is the "empirical" shell corrections of Myers and Swiatecki [27]. V_C, V_{ℓ}, and V_N are the T-dependent Coulomb, centrifugal, and nuclear proximity potentials, respectively. $\Delta R(T)$, in the definition of R_a above, is the neck-length parameter, assimilating the neck formation effects [28,29]. The choice of ΔR for a best fit to the data allows us to define the effective "barrier lowering" parameter $\Delta V_B(\ell)$ for each ℓ as the difference between the actually used barrier $V(R_a,\ell)$ and the top of the calculated barrier $V_B(\ell)$, as

$$\Delta V_B(\ell) = V(R_a,\ell) - V_B(\ell). \quad (15)$$

Note because ΔV_B is defined as a negative quantity, the actually used barrier is effectively lowered. It is relevant to point out here that, because the empirically fitted neck-length $\Delta R(T)$ is unique, the barrier lowering parameter $\Delta V_B(E_{\rm c.m.})$ is also a uniquely fixed quantity, which seems to provide favorable contribution to address data at the near- and sub-barrier regions.

III. CALCULATIONS AND RESULTS

To see the entrance channel dependence in the formation and decay of CN, calculations have been done for three different channels ^{30}Si + ^{170}Er, ^{16}O + ^{184}W, and ^{19}F + ^{181}Ta forming the same compound nucleus, i.e., ^{200}Pb*. In Sec. III A, we address the fusion cross section using the Wong and ℓ-summed extended Wong models. In Sec. III B, we study the decay mechanism in the framework of DCM. The behavior of the fragmentation path, preformation profile, average total kinetic energy, and barrier modification, etc., are investigated for a better understanding of the dynamics involved in the chosen reactions.

A. Formation of ^{200}Pb* using the Wong formula and ℓ-summed Wong model

Figure 1 shows the comparison of the fusion cross section of ^{30}Si + ^{170}Er, calculated using the Wong formula and its extended version, the ℓ-summed Wong model, with experimental data. It is clear from Fig. 1 that although the Wong formula overestimates most of the data, its extended version, after appropriate inclusion of the angular momentum

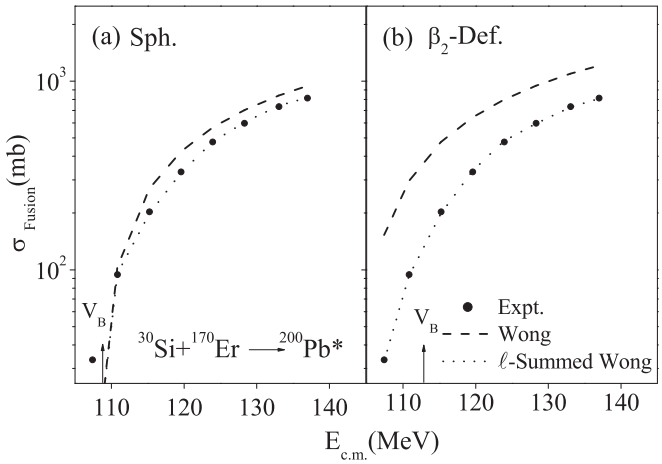

FIG. 1. Comparison of experimental data with the calculated fusion cross section using the Wong formula and its extended version, the ℓ-summed extended Wong model, for the $^{30}\mathrm{Si} + {}^{170}\mathrm{Er} \rightarrow {}^{200}\mathrm{Pb}^*$reaction with (a) spherical and (b) deformed choice of nuclei.

effect, fits the data nicely except at lowest energy for the spherical choice of fragmentation. With the inclusion of deformations, this anomaly at lowest energy gets resolved and we get a nice comparison with data at all the energies. Because barrier characteristics (V_B^ℓ, R_B^ℓ, and $\hbar\omega_\ell$), extracted from the potential barrier, are the main inputs of the Wong model and deformations modify the barrier characteristics significantly, the inclusion of deformation effects plays an appreciable role in the formation of the compound system $^{200}\mathrm{Pb}^*$.

Figures 2 and 3 are the same as that of Fig. 1 but for the $^{19}\mathrm{F} + {}^{181}\mathrm{Ta}$ and $^{16}\mathrm{O} + {}^{184}\mathrm{W}$ reactions, respectively. Figure 2 shows almost similar behavior as that of Fig. 1. However, it is observed in Fig. 3 that for the O-induced reaction, both the Wong formula and its extended version are not able to fit the data at few energies. This observation seems to suggest that there is a possibility of some nCN contribution or it may be because of the fact that $^{16}\mathrm{O}$ (projectile) and $^{200}\mathrm{Pb}$ (the CN formed) are magic nuclei, so the measured cross sections are comparatively larger for this reaction. Also, the number of target neutrons for the $^{16}\mathrm{O}$ channel are higher ($N = 110$)

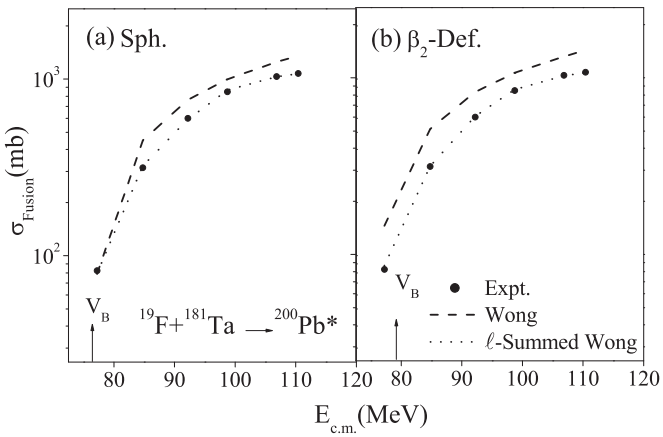

FIG. 2. Same as Fig. 1 but for the $^{19}\mathrm{F} + {}^{181}\mathrm{Ta} \rightarrow {}^{200}\mathrm{Pb}^*$ reaction.

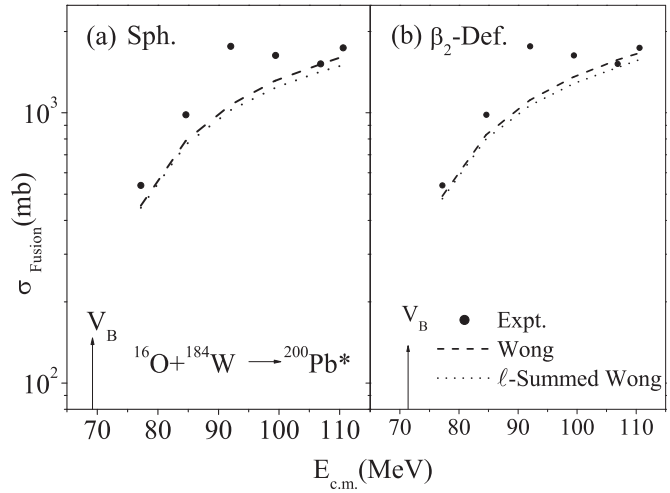

FIG. 3. Same as Fig. 1 but for the $^{16}\mathrm{O} + {}^{184}\mathrm{W} \rightarrow {}^{200}\mathrm{Pb}^*$ reaction.

than the other two incoming reactions. Therefore, the magicity associated with projectile or CN and/or higher number of neutrons in the target nucleus might be responsible for this disagreement with data.

Figure 4 shows the variation of the deduced maximum angular momentum ($\ell_{\max}$) for best fit to the experimental data as a function of $E_{\mathrm{c.m.}}$ for the spherical and deformed choice of nuclei. The $\ell_{\max}$ increases with increase in $E_{\mathrm{c.m.}}$ for all the chosen reactions. It is observed that with the inclusion of deformation, the variation becomes more smooth particularly for the $^{30}\mathrm{Si}$-induced reaction. One may recall that the comparison at lowest energy for this reaction was not good for the spherical choice of fragmentation, which improved significantly with the inclusion of deformation effects. As a result of this, we find smooth variation of $\ell_{\max}$ for the deformed case. At comparable $E_{\mathrm{c.m.}} \simeq 110$ MeV different reactions seem to give different $\ell_{\max}$ values being the least for most symmetric choice (i.e., $^{30}\mathrm{Si}$-induced reaction) and highest for the most asymmetric combination (i.e., $^{16}\mathrm{O}$-induced reaction), independent of deformation effects.

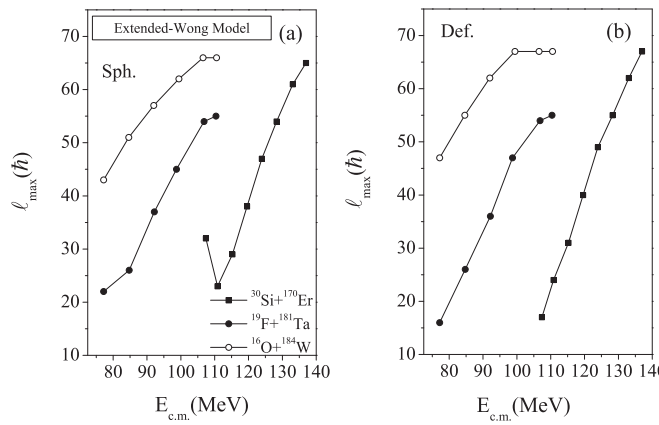

FIG. 4. Deduced $\ell_{\max}$ values as a function of $E_{\mathrm{c.m.}}$ for three incoming channels, i.e., $^{30}\mathrm{Si} + {}^{170}\mathrm{Er}$,$^{19}\mathrm{F} + {}^{181}\mathrm{Ta}$, and $^{16}\mathrm{O} + {}^{184}\mathrm{W}$ with (a) spherical and (b) deformed (up to β_2) fragmentation.

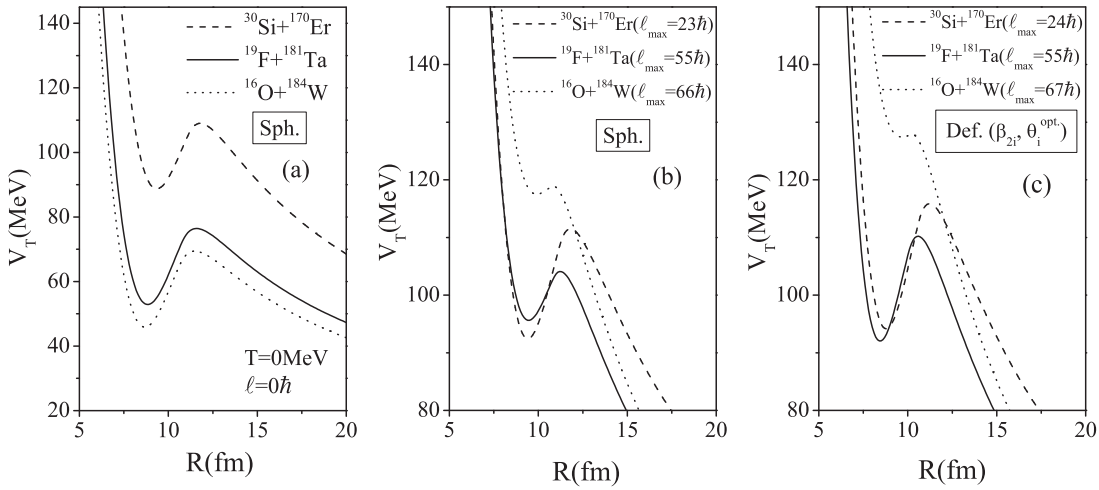

FIG. 5. Total interaction potential V_T (MeV) as a function of R (fm), for three incoming channels, i.e., $^{30}\mathrm{Si} + {}^{170}\mathrm{Er}$,$^{19}\mathrm{F} + {}^{181}\mathrm{Ta}$, and $^{16}\mathrm{O} + {}^{184}\mathrm{W}$. (a) Corresponds to spherical nuclei without temperature and angular momentum effects and (b) and (c) at $E_{\mathrm{c.m.}} \approx 110$ MeV ($T \neq 0$ and $\ell \neq 0$) for spherical and β_2 deformations, respectively.

Figure 5(a) shows the comparison of scattering potential for the three entrance channels at $T = 0$ MeV and $\ell = 0\hbar$ using spherical fragmentation. It is clear from the graph that the barrier is highest for the Si-induced channel followed by F- and O-induced reactions. The highest barrier of the Si channel finds its origin in Coulomb potential (V_c) as a product of charge numbers of target, and projectile is highest for the Si-induced reaction ($Z_1 Z_2 = 952$). The other ingredient of interaction potential, i.e., the proximity potential, on the other hand, plays a relatively silent role. Figure 5(b) shows the comparison of the total interaction potential for the three entrance channels at $E_{\mathrm{c.m.}} \approx 110$ MeV and their respective $\ell_{\max}$ values with the spherical case. It is clear from the figure that the combined effect of T and ℓ become more pronounced for the most asymmetric reaction (^{16}O) as one can observe that barrier height is almost constant for the symmetric channel ($^{30}\mathrm{Si} + {}^{170}\mathrm{Er}$) while significant change is observed in F- and O-induced reactions (asymmetric reactions). Here the highest magnitude of barrier height for $^{16}\mathrm{O} + {}^{184}\mathrm{W}$ may be associated with the larger value of $\ell_{\max}$ along with relatively higher mass asymmetry for this reaction. Figure 5(c) is the same as Fig. 5(b) but with the effect of β_2 deformation included. The comparative analysis of Fig. 5(b) with Fig. 5(c) clearly shows that the barrier characteristics are significantly influenced with the inclusion of deformation and orientation effects. Therefore one may conclude that such effects are desirable to understand the comprehensive role of the formation process using different target-projectile combinations.

Because all the reactions are forming the same compound nucleus, but behaving differently, it means different target-projectile combinations affect the compound nucleus formation. As mentioned above, the deformations and orientation also play a decisive role in the study of the fusion cross section of ^{200}Pb*. After studying the role of a different reaction partner in the formation of ^{200}Pb*, it would be of further interest to investigate the decay path of this nucleus, which is carried out in the next section.

B. Decay of ^{200}Pb* using DCM

The decay process of ^{200}Pb* formed in $^{30}\mathrm{Si} + {}^{170}\mathrm{Er}$, $^{19}\mathrm{F} + {}^{181}\mathrm{Ta}$, and $^{16}\mathrm{O} + {}^{184}\mathrm{W}$ reactions, is studied using the dynamical cluster-decay model (DCM) over a wide range of incident energies. Experimental data [1–4] of ^{30}Si-, ^{19}F-, and ^{16}O-induced reactions is available at near- and above-barrier energies. DCM gives a nice description of ER and ff cross sections with spherical and deformed choice of fragmentation by fitting only the model parameter known as the neck-length parameter "ΔR." The experimental and the DCM calculated ER and fission cross section along with the corresponding neck length and deduced maximum angular momentum at various center-of-mass energies are listed in Table I. To see the decay pattern with spherical and deformed choice of nuclei, the fragmentation potential and preformation profile are worked out at $E_{\mathrm{c.m.}} \approx 110$ MeV.

Figure 6(a) shows the comparison of fragmentation potential as a function of mass number A_2 at $E_{\mathrm{c.m.}} \approx 110$ MeV for three different entrance channels with spherical choice of fragmentation. Figure 6(b) is the same as that of Fig. 6(a) but with the effect of β_2 deformation included. Figure 6(a) shows that at $\ell = 0\hbar$ the behavior of the potential energy surface is quite similar for the three entrance channels.

However, with an increase in the ℓ value, the fragmentation behavior changes significantly. Furthermore, at $\ell = 0\hbar$, ER contribution is dominating while at $\ell_{\max}$ the symmetric fission products start competing with ER. It is observed that the magnitude of fragmentation potential is lower for $^{30}\mathrm{Si} + {}^{170}\mathrm{Er}$. It is relevant to mention here that the Q value and the asymmetry of the reaction play a significant role in deciding the decay pattern of a compound system. The change in behavior of the potential energy surface is also observed with the inclusion of deformations. Also the mode of fission distribution shifts from symmetric to asymmetric as we move from spherical to deformed choice of fragmentation. For spherical choice, the fission window is seen for $A_2 = 65$ to 100 for all the three entrance channels. However, with the inclusion of

TABLE I. The ER and Fission cross sections for the ^{200}Pb* system, calculated using the DCM at different $E_{c.m.}$'s for three different entrance channels ^{30}Si + ^{170}Er,^{19}F + ^{181}Ta,^{16}O + ^{184}W compared with the experimental data [1–4].

$E_{c.m.}$	Temp.	ΔR (fm)		$\ell_{max}(\hbar)$	$\sigma_{Expt.}$(mb)		σ_{DCM}(mb)	
(MeV)	(MeV)	ER	Fission		ER	Fission	ER	Fission
			^{30}Si + ^{170}Er → ^{200}Pb* (Q_{in} = −58.308 MeV)					
107.40	1.508	1.682	0.710	123	31.98	1.37	31.30	1.382
110.84	1.560	1.750	0.878	125	80.08	14.41	81.30	14.68
115.24	1.623	1.796	1.007	127	140.33	63.17	139.0	63.60
119.57	1.683	1.843	1.080	127	202.34	128.34	201.0	128.6
123.93	1.741	1.841	1.154	129	217.34	259.80	216.0	260.0
128.31	1.797	1.838	1.195	130	216.34	382.30	216.0	382.0
133.06	1.856	1.835	1.214	131	210.0	523.91	210.0	522.0
136.96	1.903	1.834	1.231	131	202.34	611.29	202.0	612.0
			^{19}F + ^{181}Ta → ^{200}Pb* (Q_{in} = −23.689 MeV)					
77.21	1.5745	1.726	0.784	124	77.08	5.16	77.8	5.23
84.75	1.6802	1.865	0.990	126	313.97	61.35	314.0	61.40
92.19	1.7783	1.887	1.104	128	396.78	203.62	396.0	204.0
98.72	1.8601	1.900	1.193	129	425.64	423.16	425.0	424.0
106.84	1.9570	1.884	1.216	132	401.45	633.66	400.0	626.0
110.40	1.9979	1.864	1.227	133	342.78	733.48	342.0	734.0
			^{16}O + ^{184}W → ^{200}Pb* (Q_{in} = −24.204 MeV)					
77.19	1.5668	1.938	0.891	124	521.50	23.68	523.0	22.8
84.61	1.6713	1.997	1.05	125	861.81	121.17	789.0	121.0
92.02	1.7695	2.075	1.151	128	1473.38	318.80	1470.0	320.0
99.43	1.8625	2.04	1.20	130	1153.96	498.99	1150.0	502.0
106.86	1.9512	2.0	1.223	131	853.08	677.26	850.0	678.0
110.56	1.9939	2.035	1.227	132	1067.28	698.27	1070.0	698.0

deformations the fragmentation profile changes significantly particularly in the fissioning region. The Si-induced reaction exhibits a double humped structure where symmetric as well asymmetric dips are distinctly visible, respectively, at A_2 = 58 to 84 and A_2 = 91 to 100. On the other hand F-induced and O-induced reactions show prominence of an asymmetric fission window with an almost negligible contribution of symmetric fragments. This point is emphasized further in the behavior of the preformation factor depicted in Fig. 7.

It is clear from Fig. 7 that the behavior of preformation probability P_0^{ℓ} with fragment mass A_2 is symmetric for the spherical choice of fragment, however, it shifts to asymmetric fission for the deformed choice of fragments. For simplicity

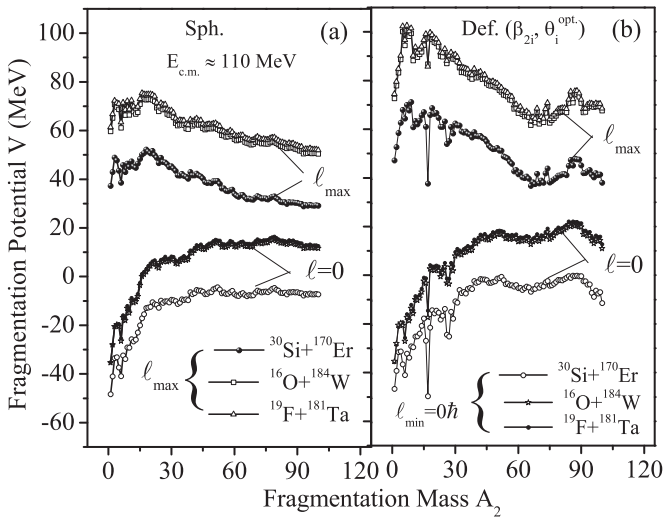

FIG. 6. Fragmentation potential V (MeV) as a function of fragment mass A_2 at fixed $E_{c.m.}$ for three entrance channels with (a) spherical and (b) deformed choice of fragmentation. (For ℓ_{max} see Table I.)

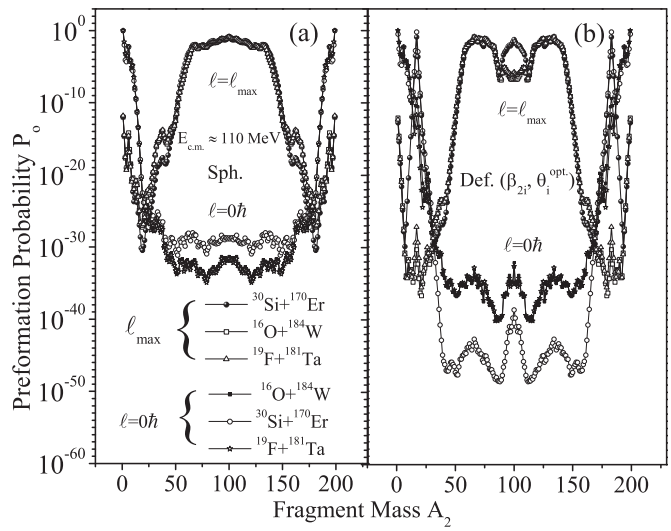

FIG. 7. Preformation probability P_0 as a function of fragment mass A_2 for three different incoming channels for (a) spherical and (b) deformed choice of nuclei. (For ℓ_{max} see Table I.)

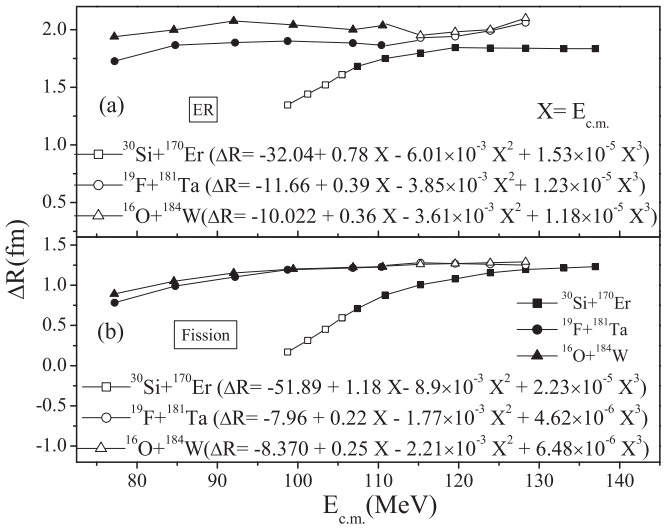

FIG. 8. Neck-length parameter ΔR as a function of $E_{\text{c.m.}}$ for spherical choice of nuclei of CN ^{200}Pb* formed by using three entrance channels. Filled and open symbols mark calculations with DCM and predicted values of ΔR by polynomial fitting of order three, respectively, for (a) ER and (b) fission cross section.

P_0^{ℓ} is marked as P_0 in the subsequent discussion. Although the behavior of preformation probability with A_2 is similar for all three reactions for spherical choice of fragments, the same is not true for deformed fragmentation. From Fig. 7(b) one can clearly observe that the preformation profile of the ^{30}Si channel is quite different than that for ^{19}F- and ^{16}O-induced reactions. Therefore, it is evident that the deformation and orientation degree of freedom play an important role in the decay mechanism of ^{200}Pb* and entrance channel dependence seems evident in the deformed fragmentation process. Henceforth one may conclude that by varying the target-projectile combination, significant modification is observed in the decay path of the ^{200}Pb* nucleus.

TABLE II. Predicted ER and fission cross sections for the ^{200}Pb* system by polynomial fitting of order 3, using the DCM at different $E_{\text{c.m.}}$'s for three different entrance channels ^{30}Si + ^{170}Er,^{19}F + ^{181}Ta, and ^{16}O + ^{184}W.

$E_{\text{c.m.}}$	Temp.	ΔR (fm)		$\ell_{\max}(\hbar)$	σ_{DCM}(mb)	
(MeV)	(MeV)	ER	Fission		ER	Fission
			^{30}Si + ^{170}Er → ^{200}Pb*			
98.72	1.3663	1.345	0.170	121	0.198	2.16×10^{-3}
101.21	1.412	1.44	0.315	121	0.902	1.13×10^{-2}
103.42	1.447	1.52	0.453	122	3.42	7.68×10^{-2}
105.47	1.479	1.61	0.595	123	13.2	4.82×10^{-1}
			^{19}F + ^{181}Ta → ^{200}Pb*			
115.24	2.052	1.93	1.28	134	549.0	940.0
119.57	2.099	1.94	1.27	134	552.0	882.0
123.93	2.146	1.99	1.26	135	830.0	788.0
128.31	2.192	2.06	1.25	135	1150.0	722.0
			^{16}O + ^{184}W → ^{200}Pb*			
115.24	2.046	1.95	1.26	131	476.0	860.0
119.57	2.094	1.98	1.27	135	803.0	884.0
123.93	2.141	2.00	1.28	138	1060.0	886.0
128.31	2.187	2.10	1.29	136	1050.0	842.0

Figure 8 shows the variation of the neck-length parameter ΔR as a function of $E_{\text{c.m.}}$ for the ER [Fig. 8(a)] and fission cross section [Fig. 8(b)] for the chosen entrance channels using spherical choice of fragmentation. The comparison of Figs. 8(a) and 8(b) clearly show that ΔR for the ER process is higher than that for fission, independent of the choice of entrance channel. Using the systematics of ΔR values for experimental data, the neck-length parameter ΔR is extrapolated by using polynomial fitting of order 3. In other words we have estimated the ΔR values for energies above

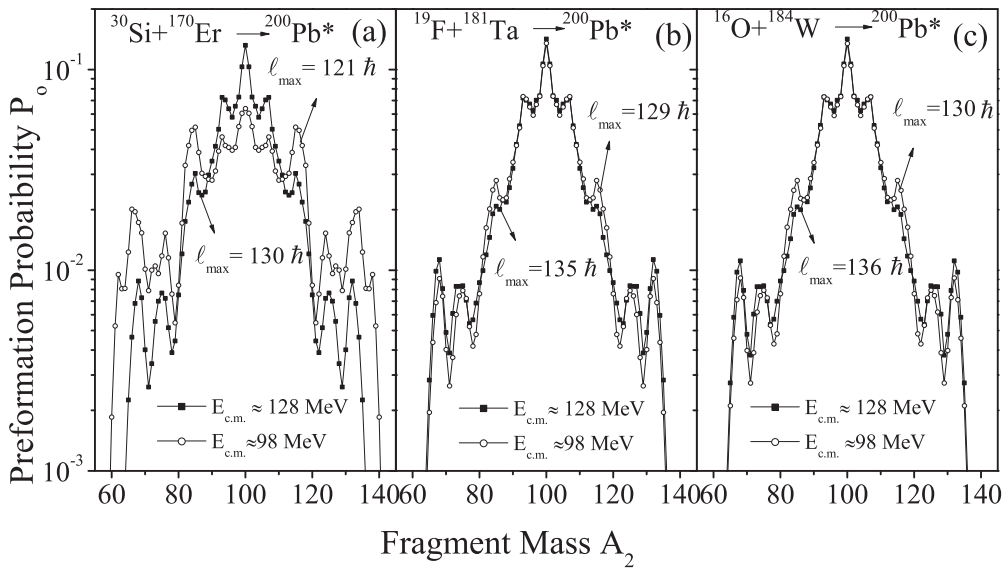

FIG. 9. Preformation probability P_0 as a function of fragment mass A_2 plotted at $E_{\text{c.m.}}$ = 98 MeV and 128 MeV for (a) ^{30}Si + ^{170}Er, (b) ^{19}F + ^{181}Ta, and (c) ^{16}O + ^{184}W reactions.

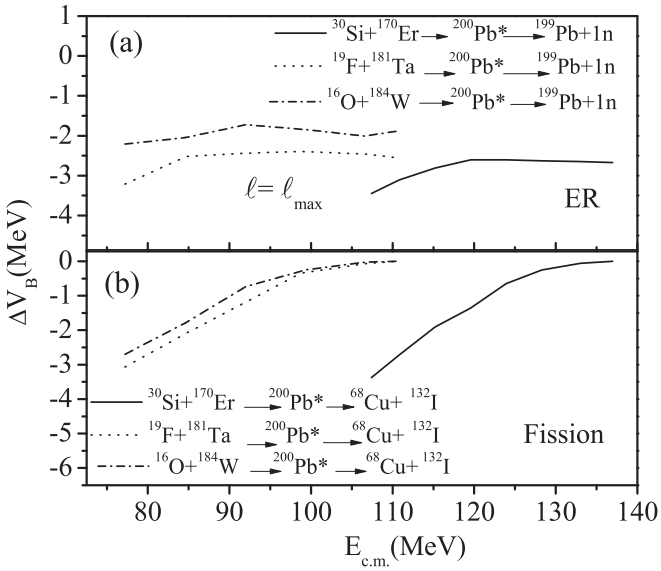

FIG. 10. Barrier-lowering parameter ΔV_B as a function of $E_{\text{c.m.}}$ for highest contributing fragments at $\ell = \ell_{\max}$ (a) ER and (b) fission.

110 MeV for ^{16}O- and ^{19}F-induced reactions and energies below 107 MeV for the relatively symmetric ^{30}Si-induced channel, so as to obtain cross sections in the energy range $E_{\text{c.m.}} = 98$–128 MeV for all three channels. The filled symbols in Fig. 8 correspond to fitted ΔR values in reference to data of [1–4], and the open symbols correspond to the extrapolating ΔR values obtained using the polynomial fitting. The corresponding cross sections and ℓ values are predicted and the same are listed in Table II. An experimental verification is called for these predicted cross sections. The main purpose of extrapolation of ΔR in Fig. 8 is to provide the ER and fission cross section in a comprehensive energy range, i.e., $E_{\text{c.m.}} =$ 98–128 MeV.

To study the temperature dependence on decay structure of ^{200}Pb*, comparison of the preformation profile P_0 is made at extreme common energies, i.e., at 98 MeV and 128 MeV, respectively, using spherical fragmentation for all three channels. If we see Fig. 7(a), symmetric fragment contribution is evident for all the chosen reactions. However, from Fig. 9 it is clear that although the structure is almost the same at extreme energies, a significant difference in magnitude is observed in the Si channel as shown in Fig. 9(a). It means that the effect of energy is more prominent in the symmetric channel as compared to asymmetric channels [Figs. 9(a) and 9(b)]. Clearly, the extrapolation of the neck-length parameter and consequent prediction of data can be exploited to have a better understanding of the fission dynamics of ^{200}Pb*. The barrier modification effect is also worked out as an in-built property of the fitting parameter, the neck-length parameter ΔR. The barrier modification ΔV_B depends upon the barrier height V_B and barrier penetration point $V(R_a)$ as shown in Eq. (15). Figures 10(a) and 10(b) show the variation of the barrier lowering parameter ΔV_B as a function of $E_{\text{c.m.}}$ for ER and fission cross sections, respectively. One may clearly see that ΔV_B variation follows the trend of the neck-length

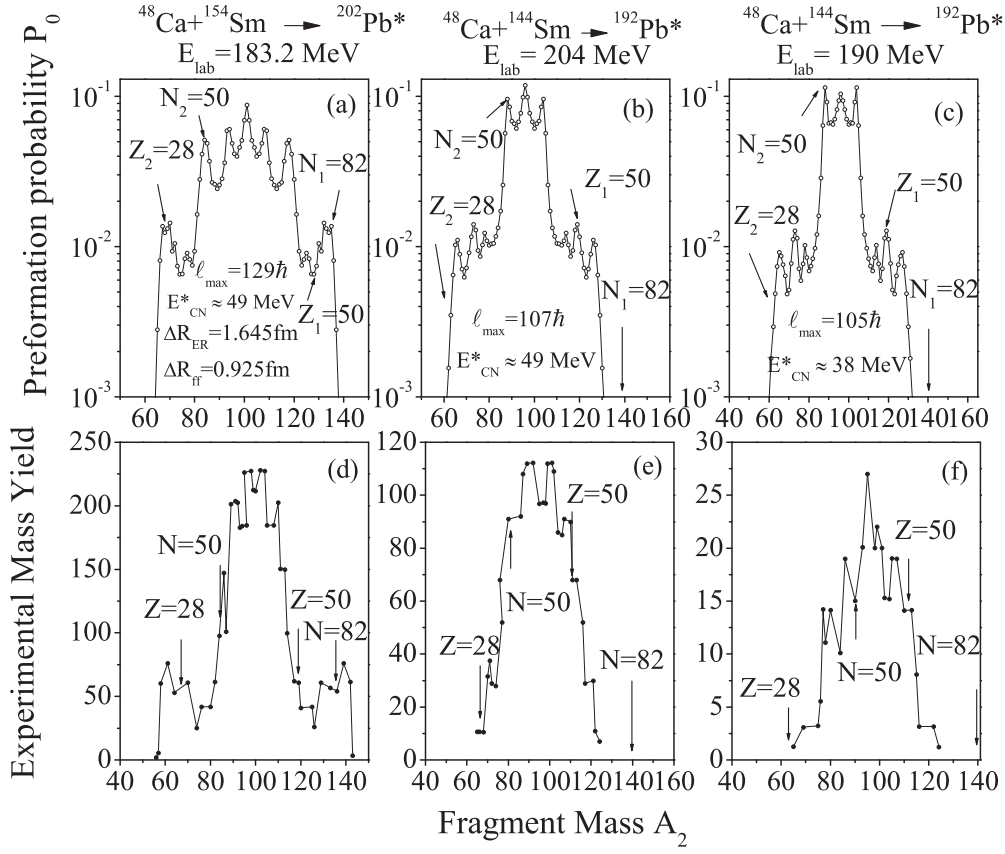

FIG. 11. Preformation probability P_0 (upper panel) and experimental mass yield (lower panel), plotted as a function of fragment mass A_2.

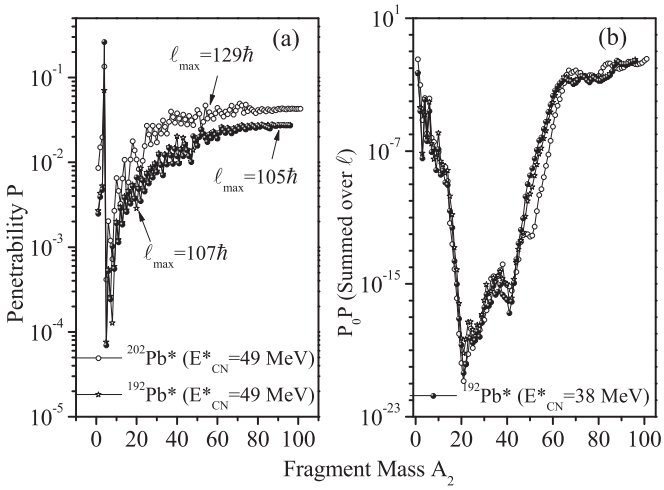

FIG. 12. (a) Penetrability P at $\ell = \ell_{max}$ and (b) the ℓ-summed $P_0^\ell P_\ell$ as a function of fragment mass A_2 for two incoming channels.

parameter "ΔR" depicted in Fig. 8. Henceforth, it is evident that barrier modification is an in-built parameter in DCM, which is uniquely fixed in reference to ΔR values and is of huge importance to address the data particularly at near- and below-barrier regions.

Finally, to study the behavior of different isotopes around the ^{200}Pb* region, ^{192}Pb* and ^{202}Pb* nuclei formed by using ^{48}Ca + ^{144,154}Sm reactions are investigated in the framework of DCM. Preformation probability P_0 (equivalently the mass yield), penetrability P and average total kinetic energy ⟨TKE⟩ are calculated for decaying fragments of the above mentioned reactions at E_{lab} = 183.2 MeV for ^{202}Pb* and at E_{lab} = 204 MeV, 190 MeV for ^{192}Pb*. The available evaporation residue and fission data [30,31] of the ^{48}Ca + ^{154}Sm $\rightarrow$ ^{202} Pb* $\rightarrow$ A$_1$ + A$_2$ reaction is addressed by taking ΔR_{ER}= 1.645 fm and ΔR_{ff} = 0.925 fm. Because no experimental data are available for the ^{48}Ca + ^{144}Sm reaction, the same neck length is used for calculating preformation probability P_0, penetrability P, and ⟨TKE⟩. The relatively higher values of angular momentum ℓ_{max} are from the moment of inertia in the sticking limit (for further details see Ref. [32]). Because nuclear structure effects appear in DCM via preformation probability P_0, the structural pattern of experimental mass yield is compared with P_0, in Fig. 11. The preformation factor of ^{202}Pb* at E^*_{CN} = 49 MeV is shown in Fig. 11(a) and that for ^{192}Pb* at E^*_{CN} = 49 MeV and E^*_{CN} = 38 MeV in Figs. 11(b) and 11(c), respectively. A near symmetric mass distribution is observed, with emergence of shoulders corresponding to magic shells at Z_2 = 28, N_2 = 50, and N_1 = 82. These secondary peaks are relatively suppressed for the neutron deficient ^{192}Pb* nucleus in agreement with [33,34]. The preformation probability plotted in the upper panel of Fig. 11 finds nice comparison with the structural distribution of mass yields plotted in the lower panel. Figure 12(a) shows the barrier penetrability P as a function of fragment mass A_2 at maximum angular momentum for two channels. It imparts the following information. (i) The penetrability P of light mass fragments particularly for the α particle is significantly large. (ii) In general P increases as a function of fragment mass and starts saturating in the fission region. (iii) Independent of entrance channel effect the α nucleus structure is visible in the IMF and HMF regions, which start disappearing in the fission window. In Fig. 12(b), summed up $P_0^\ell P_\ell$ is plotted as a function of fragment mass A_2 for two incoming channels i.e. ^{48}Ca+^{154}Sm at E^*_{CN} = 49 MeV and ^{48}Ca+^{144}Sm at E^*_{CN} = 49 and 38 MeV. In other words, for each fragment, the ℓ summation of $P_0^\ell P_\ell$ is worked out over all contributing angular momentum values up to ℓ_{max} to demonstrate the collective role of these quantities. It is observed that the product $P_0^\ell P_\ell$ provide an interesting structure as a function

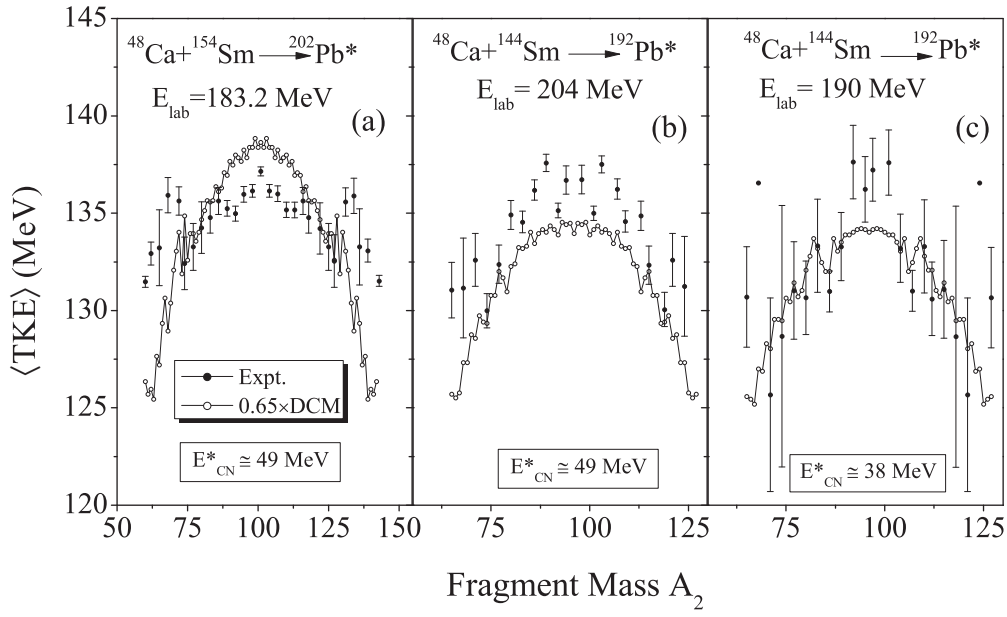

FIG. 13. Average total kinetic energy ⟨TKE⟩ and available experimental data plotted as a function of fragment mass A_2.

of fragment mass A_2. One may notice that this structural distribution is mainly influenced and via the preformation profile as the penetrability contributes mainly towards the magnitude as described in our earlier work [35]. A closer look at Fig. 12(b) clearly shows that the ER and fission cross sections compete with each other as the $P_0^\ell P_\ell$ product is highest for these fragments. This observation is in agreement with measured data of Ref. [30,31]. The chosen reaction channels seem to impart similar behavior for the ER to fission regions.

In Fig. 13, the average total kinetic energy ⟨TKE⟩ of two systems is plotted as fragment mass A_2. The calculated ⟨TKE⟩ is higher in magnitude, which suggests that comparatively smaller ℓ values contribute towards ⟨TKE⟩ calculations, as depicted in Refs. [36,37]. So to compare the DCM calculated ⟨TKE⟩ values with experimental data, a scaling factor of 0.65 is used as shown in Fig. 13. After rescaling, the calculated ⟨TKE⟩ seem to provide reasonable comparison with the experimental data.

IV. SUMMARY

We have studied the formation and decay process of ^{200}Pb* formed via three different entrance channels, i.e., ^{30}Si + ^{170}Er, ^{19}F + ^{181}Ta, and ^{16}O + ^{184}W. Calculations have been done in the framework of the Wong model and DCM to investigate, respectively, the fusion and decay process of ^{200}Pb* using spherical and deformed choice of fragments. The ℓ-summed Wong model is shown to give reasonable description of experimental data and deformation effects are shown to influence the formation process of the ^{200}Pb* nucleus. The entrance channel dependence is explored in the context of deformation and angular momentum effects. On the other hand, the dynamical cluster decay approach is used to give a description of ER and fission cross sections over a wide range of incident energies, by empirically fitting the neck-length parameter ΔR, which incorporates the neck formation effects. The deformations and orientation effects are shown to play a significant role in the decay process as well. In addition to this, some signature of entrance channel dependence is seen in the deformed fragmentation process of the ^{200}Pb* nucleus. The ER and fission cross sections are predicted for all three channels. An experimental verification is called for predicted cross sections in energy range $E_{\rm c.m.} = 98$–128 MeV. Finally the behavior of neighboring isotopes ^{192}Pb* and ^{202}Pb* is analyzed in terms of total average kinetic energy, penetrability, and mass yield distribution patterns.

ACKNOWLEDGMENTS

Financial support from the University Grant Commission (UGC), Ref. No. 41-978/(2012)(SR), New Delhi, is gratefully acknowledged. One of us (R.K.) acknowledges financial support from University of Padova, Italy.

[1] D. J. Hinde, J. R. Leigh, J. O. Newton, W. Galster, and S. Sie, Nucl. Phys. A **385**, 109 (1982).
[2] G. Mohanto *et al.*, Nucl. Phys. A **890-891**, 62 (2012).
[3] P. D. Shidling *et al.*, Phys. Rev. C **74**, 064603 (2006).
[4] J. S. Forster, I. V. Mitchell, J. U. Andersen, A. S. Jensen, E. Laegsgaard, W. M. Gibson, and K. Prichett, Nucl. Phys. A **464**, 497 (1987).
[5] C. Y. Wong, Phys. Rev. Lett. **31**, 766 (1973).
[6] R. Kumar, M. Bansal, S. K. Arun, and R. K. Gupta, Phys. Rev. C **80**, 034618 (2009).
[7] R. Kumar, Phys. Rev. C **84**, 044613 (2011).
[8] D. Jain, R. Kumar, M. K. Sharma, and R. K. Gupta, Phys. Rev. C **85**, 024615 (2012).
[9] D. Jain, R. Kumar, and M. K. Sharma, Phys. Rev. C **87**, 044612 (2013).
[10] B. B. Singh, M. K. Sharma, and R. K. Gupta, Phys. Rev. C **77**, 054613 (2008).
[11] R. Kumar and R. K. Gupta, Phys. Rev. C **79**, 034602 (2009).
[12] R. K. Gupta, in *Cluster in Nuclei*, Lecture Notes in Physics 818, Vol. I, edited by C. Beck (Springer-Verlag, Berlin, 2010), p. 223.
[13] R. K. Gupta, S. K. Arun, R. Kumar, and M. Bansal, Nucl. Phys. A **834**, 176c (2010).
[14] M. K. Sharma, S. Kanwar, G. Sawhney, R. K. Gupta, and W. Greiner, J. Phys. G: Nucl. Part. Phys. **38**, 055104 (2011).
[15] M. Kaur, R. Kumar, and M. K. Sharma, Phys. Rev. C **85**, 014609 (2012).
[16] K. Sandhu, M. K. Sharma, and R. K. Gupta, Phys. Rev. C **85**, 024604 (2012).
[17] G. Kaur and M. K. Sharma, Phys. Rev. C **87**, 044601 (2013).
[18] M. Kaur and M. K. Sharma, Phys. Rev. C **85**, 054605 (2012).
[19] G. Sawhney, R. Kumar, and M. K. Sharma, Phys. Rev. C **86**, 034613 (2012).
[20] G. Kaur, D. Jain, R. Kumar, and M. K. Sharma, Nucl. Phys. A **916**, 260 (2013).
[21] R. Kumar, K. Sandhu, M. K. Sharma, and R. K. Gupta, Phys. Rev. C **87**, 054610 (2013).
[22] R. K. Gupta, M. Balasubramanium, R. Kumar, N. Singh, M. Manhas, and W. Greiner, J. Phys. G: Nucl. Part. Phys. **31**, 631 (2005).
[23] D. L. Hill and J. A. Wheeler, Phys. Rev. **89**, 1102 (1953); T. D. Thomas, *ibid.* **116**, 703 (1959).
[24] G. Royer and J. Mignen, J. Phys. G: Nucl. Part. Phys. **18**, 1781 (1992).
[25] P. Möller, J. R. Nix, W. D. Myers, and W. J. Swiatecki, At. Nucl. Data Tables **59**, 185 (1995).
[26] N. J. Davidson, S. S. Hsiao, J. Markram, H. G. Miller, and Y. Tsang, Nucl. Phys. A **570**, 61 (1994).
[27] W. Myers and W. J. Swiatecki, Nucl. Phys. A **81**, 1 (1966).
[28] S. Kumar and R. K. Gupta, Phys. Rev. C **55**, 218 (1997).
[29] H. S. Khosla, S. K. Malik, and R. K. Gupta, Nucl. Phys. A **513**, 115 (1990).
[30] A. M. Stefanini *et al.*, Eur. Phys. J. A **23**, 473 (2005).
[31] G. N. Knyazheva *et al.*, Phys. Rev. C **75**, 064602 (2007).
[32] G. Sawhney, R. Kumar, Rajni, and M. K. Sharma, AIP. Conf. Proc. **1524**, 174 (2013).
[33] M. G. Itkis *et al.*, Nucl. Phys. A **734**, 136 (2004).
[34] S. Kanwar *et al.*, Int. J. Mod. Phys. E **18**, 1453 (2009).
[35] M. Sharma *et al.*, J. Phys. G: Nucl. Part. Phys. **38**, 105101 (2011).
[36] K. Sandhu, G. Kaur, and M. K. Sharma, Nucl. Phys. A **921**, 114 (2014).
[37] B. B. Singh *et al.*, Int. J. Mod. Phys. E **15**, 699 (2006).